Acta Cryst A
FOUNDATIONS
ADVANCES

ISSN 2053-2733

Received 26 July 2018
Accepted 1 May 2019

Edited by L. D. Marks, Northwestern University, USA

Keywords: manganese Ruddlesden–Popper-related phases; oxygen vacancies; atomic resolution.

Supporting information: this article has supporting information at journals.iucr.org/a

Complex structural ordering of the oxygen deficiency in $La_{0.5}Ca_{2.5}Mn_2O_{7-\delta}$ Ruddlesden–Popper phases

Daniel González-Merchante,[a] Raquel Cortés-Gil,[a] José M. Alonso,[b,c] Emilio Matesanz,[d] José L. Martínez,[b] Alberto Rivera-Calzada,[e] Jacobo Santamaría,[e] M. Luisa Ruiz-González[a] and José M. González-Calbet[a,f]*

[a]Departamento de Química Inorgánica, Facultad de Químicas, Universidad Complutense (UCM), CEI Moncloa, Madrid 28040, Spain, [b]Instituto de Ciencia de Materiales, CSIC, Sor Juana Inés de la Cruz s/n, Madrid 28049, Spain, [c]Instituto de Magnetismo Aplicado, UCM-CSIC-ADIF, PO Box 155, Madrid, Las Rozas 28230, Spain, [d]CAI de Difracción de Rayos X, UCM, CEI Moncloa, Madrid 28040, Spain, [e]Departamento de Física de los Materiales, Facultad de Físicas, UCM CEI Moncloa, Madrid 28040, Spain, and [f]Centro Nacional de Microscopia Electrónica, UCM, CEI Moncloa, Madrid 28040, Spain. *Correspondence e-mail: jgcalbet@ucm.es

Ruddlesden–Popper oxides, $(AO)(ABO_3)_n$, occupy a prominent place in the landscape of materials research because of their intriguing potential applications. Compositional modifications to the cation sublattices, A or B, have been explored in order to achieve enhanced functionalities. However, changes to the anionic sublattice have been much less explored. In this work, new oxygen-deficient manganese Ruddlesden–Popper-related phases, $La_{0.5}Ca_{2.5}Mn_2O_{6.5}$ and $La_{0.5}Ca_{2.5}Mn_2O_{6.25}$, have been synthesized by controlled reduction of the fully oxidized $n = 2$ term $La_{0.5}Ca_{2.5}Mn_2O_7$. A complete structural and compositional characterization, by means of neutron diffraction, electron diffraction and atomically resolved scanning transmission electron microscopy and electron energy-loss spectroscopy techniques, allows the proposition of a topotactic reduction pathway through preferential oxygen removal in the $[MnO_2]$ layers along [031] and $[0\bar{1}3]$ directions. The gradual decrease of the Mn oxidation state, accommodated by short-range ordering of anionic vacancies, reasonably explains the breaking of ferromagnetic interactions reinforcing the emergence of antiferromagnetic ones. Additional short-range order–disorder phenomena of La and Ca cations have been detected in the reduced $La_{0.5}Ca_{2.5}Mn_2O_{7-\delta}$, as previously reported in the parent compound.

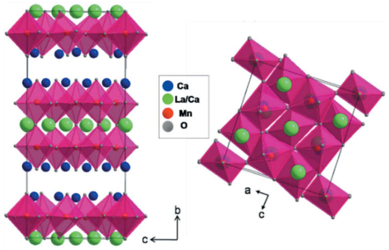

1. Introduction

Ruddlesden–Popper (RP) oxides have attracted a lot of attention since they exhibit magnetoresistance (MR) and other exciting behaviours like ferroelectric, piezoelectric, magnetic, superconducting and catalytic properties (Jeyalakshmi *et al.*, 2015; Lee *et al.*, 2013; Massee *et al.*, 2011; Moritomo *et al.*, 1996; Mulder *et al.*, 2013). In order to understand the outstanding properties of these $(AO)(ABO_3)_n$ oxides, one first needs to visualize the structure, which is the result of ordered intergrowth between n (ABO_3) perovskite (P) blocks and one (AO) rock-salt (RS) layer. This ordered arrangement of different chemical and structural units induces intriguing features that can be modified by controlling the number of intergrowing perovskite units. However, the main disadvantage of this approach is the difficulty of stabilizing high n members, which are frequently obtained as disordered intergrowths between the basic perovskite units, unless a controlled layer-by-layer physical method is used (Lee *et al.*, 2014; Rijnders, 2014; Yan *et al.*, 2007). Most studies, either of thin films or polycrystalline compounds, have been mainly focused on the effect of the cation composition (Battle, Green *et al.*, 1997) and comparatively less effort has been devoted to the control of oxygen stoichiometry.

Regarding the $n = 2$ term, the fully oxidized $A_3B_2O_7$ compound comprises the intergrowth of two P units and one RS layer, as depicted in Fig. S1 in the supporting information. In the case of reduced $A_3B_2O_{7-\delta}$, two oxygen vacancy arrangements have been described for different compositions according to two patterns: (i) a pattern of oxygen vacancies located in the middle of the double P layers (marked in Fig. S1 as apical oxygen), and (ii) a pattern of oxygen vacancies located in the equatorial sites (marked in Fig. S1 as equatorial oxygen), which means in the BO_2 planes along the [110] and $[1\bar{1}0]$ directions. In both cases, square-pyramid polyhedra are formed and could give rise to new, ordered superlattices along [001] (i) and $\langle 110 \rangle$ (ii) as represented schematically in Figs. S1(*c*) and S1(*d*). For instance, the first pattern was initially observed for the superconducting $La_{2-x}Sr_{1+x}Cu_2O_6$ oxide (Nguyen *et al.*, 1980), built up of square pyramids sharing corners due to the ordered removal of the octahedral apical sites. This ordered arrangement has also been found (Dann & Weller, 1995) in $Sr_3Co_2O_6$ and, more recently, in Mn-based compounds (El Shinawi *et al.*, 2010). For intermediate oxygen stoichiometries, the same pattern of vacancies, although with different degrees of occupancy, has been described in the cobalt and copper systems (Lucas *et al.*, 1992; Viciu *et al.*, 2006). Notice that all these phases are obtained at room pressure or even using oxidant conditions, as it is difficult to reach the full oxygen lattice content, O_7, due to the copper and cobalt oxidation states. In contrast, for manganese oxides it is possible to prepare the fully oxidized phase, which can then be topotactically reduced. The accommodation of oxygen non-stoichiometry in $Sr_3Mn_2O_{7-\delta}$ oxides takes place along the MnO_2 layers at the equatorial sites (see Fig. S1) (Gillie *et al.*, 2003; Mitchell *et al.*, 1998), giving rise to a superlattice along [110] and equivalent directions as marked in Fig. S1(*d*), as previously observed in $CaMnO_{3-\delta}$ perovskite (Reller *et al.*, 1984) and $Ca_2MnO_{3.5}$ reduced compounds (Poeppelmeier *et al.*, 1982).

In terms of the MR properties, the most interesting behaviour in an RP system has been found in $n = 2$ $Ln_{2-x}AE_{1+2x}Mn_2O_7$ (Ln = lanthanide; AE = Ca, Sr) manganites (Battle, Cox *et al.*, 1997; Lee, Kao *et al.*, 2011; Ling *et al.*, 2000). The MR effects are mainly ascribed to Sr systems while order phenomena, such as charge (CO), orbital and anti-ferromagnetic (AFM) ordering, have been described for the Ca one (Fawcett *et al.*, 2000). The reduction of oxygen content in $n = 2$ RP has been mainly focused on $AE_3B_2O_7$-related compositions, while less attention has been paid to when Ln partially substitutes AE. This is probably due to the difficulty of isolating single phases in the more complex $(LnAE)_3B_2O_7$ systems (Battle, Green *et al.*, 1997). The two oxygen vacancy patterns, described above, have also been described in these complex oxides (Hayward, 2006, 2014; Millburn & Mitchell, 2001; Zurita-Blasco *et al.*, 2007). For instance, for $Nd_{2-2x}Sr_{1-2x}Mn_3O_7$ (Millburn & Mitchell, 2001) and $LaBa_2Mn_3O_7$ (Zurita-Blasco *et al.*, 2007) compounds, vacancies are placed at the apical site in the P block, while they occur at the equatorial sites, along [011], in the $YSr_2MnO_{5.5}$ reduced phase (Hayward, 2006, 2014). In addition, RP reduced oxyhalides have also been reported (Hayward, 2014). All of the above compounds have been obtained from topotactic reduction of the fully oxidized phases. Nevertheless, a systematic study of the gradual reduction pathway has not been performed. Furthermore, it is worth mentioning that fully oxidized phases, free of disordered intergrowths, are usually difficult to stabilize for $n \geq 2$. A mixture of reduced phases has also been obtained (Millburn & Mitchell, 2001). In this context, the aim of this work is to systematically study the influence of the oxygen reduction process on the structural and physical behaviour of the previously unexplored $La_{0.5}Ca_{2.5}Mn_2O_{7-\delta}$ (δ = 0, 0.5, 0.75) system. For that purpose, we have carried out the reduction process of the highly homogeneous $n = 2$ $La_{0.5}Ca_{2.5}Mn_2O_7$ member, recently reported by Ruiz-González *et al.* (2015). It contains micrometric particles with an outstanding ordered distribution of two P and one RS units, ideal for studying the accommodation of oxygen vacancies.

2. Experimental

2.1. Synthesis of $La_{0.5}Ca_{2.5}Mn_2O_{7-\delta}$ (δ = 0, 0.5, 0.75) phases

The starting material, $La_{0.5}Ca_{2.5}Mn_2O_7$, for the reduction process was prepared by using the ceramic method with special care taken during the cooling process, using a very slow cooling rate of 0.1 K min^{-1} in order to avoid the presence of disordered intergrowths (Ruiz-González *et al.*, 2015). Once this sample was obtained, the reduction processes were performed inside a CAHN D-200 electrobalance equipped with a furnace and a two-channel register. The starting material was heated under a reducing H_2 (2×10^4 Pa) and He (3×10^4 Pa) atmosphere, at a rate of 6 K min^{-1} until 623 K. Once this temperature was reached, the heating rate was decreased to 1 K min^{-1}, and the heating process maintained until the desirable oxygen content was obtained. The target temperatures were 733 and 748 K for $La_{0.5}Ca_{2.5}Mn_2O_{6.5}$ and $La_{0.5}Ca_{2.5}Mn_2O_{6.25}$, respectively. The samples were finally quenched at room temperature. The thermogravimetric curves are shown in Fig. S2.

2.2. Chemical analysis determination by electron probe microanalysis (EPMA) and X-ray energy-dispersive spectroscopy (EDS)

Cation compositional analysis was determined by means of EPMA, attached to a JEOL JXA-8900 microscope, analysing around 20 areas of 1–5 µm in size. In addition, the cation ratio was always analysed in each particle, prior to the selected-area electron diffraction (SAED) and high-resolution transmission electron microscopy (HRTEM), by means of EDS.

2.3. X-ray (XRD) and neutron diffraction (ND) characterization

XRD was performed using a PANalytical X'pert PRO diffractometer operating with Cu $K\alpha_1$ radiation in Bragg–Brentano geometry at room temperature. ND measurements at room temperature were performed using the diffractometer D2B (Institut Laue–Langevin, Grenoble) with λ = 1.5943 Å. The crystal structure was refined by the Rietveld method using the *FullProf* software (Rodríguez-Carvajal, 1993). In order to explore compatible symmetries, the resulting unit cell was analysed with the aid of the *FINDSYM* program (Stokes & Hatch, 2005).

2.4. Electron microscopy characterization

SAED and HRTEM were performed on a JEOL JEM 300FEG electron microscope equipped with an EDS microanalysis system (Oxford INCA). Atomic scale characterization was done in a JEOL JSM-ARM200cF electron microscope (cold emission gun) provided with a spherical aberration corrector in the probe (current emission density $\sim 1.4 \times 10^{-9}$ A and probe size ~0.8 Å operated at 200 kV), a GIF-QuantumERTM spectrometer and an Oxford INCA-350 detector.

2.5. Magnetic properties

The magnetic susceptibility and magnetization were measured with a SQUID magnetometer from Quantum Design with an external magnetic field up to 14 T and temperature range from 2 to 400 K. The temperature-dependence resistance measurements were performed using the standard four-probe method in the temperature range 5–350 K under 0 and 14 T applied magnetic field.

2.6. Electrical conductivity

Conductivity was measured by alternating current methods using Novocontrol BDS80 impedance spectroscopy equipment. Contacts were silver epoxy pads on the surface of cylindrical cold-pressed pellets. Measurements were conducted under an inert N_2 flow. Temperature was varied between 125 and 500 K. DC conductivity was obtained from the low-frequency plateaus of conductivity versus frequency spectra measured in the range 100 mHz–10 MHz.

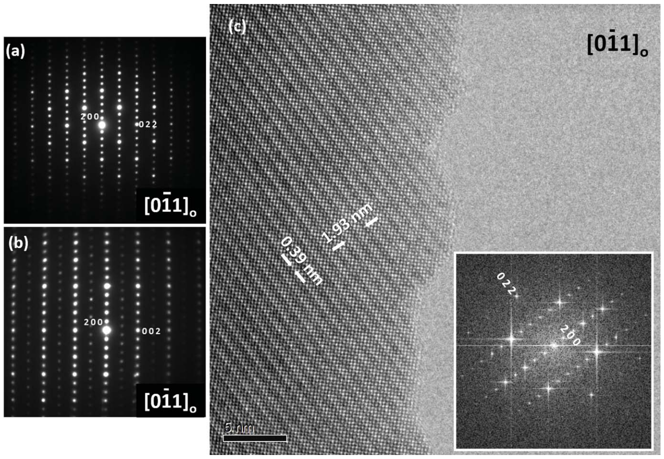

Figure 1
SAED pattern corresponding to $La_{0.5}Ca_{2.5}Mn_2O_{6.5}$ along (*a*) $[0\bar{1}1]_o$ and (*b*) [010]; (*c*) HRTEM image of $La_{0.5}Ca_{2.5}Mn_2O_{6.5}$ along $[0\bar{1}1]_o$. The inset shows the corresponding fast Fourier transform.

3. Results and discussion

Thermogravimetric curves corresponding to the reduction processes are shown in Fig. S2. XRD patterns for the three samples are quite similar (Fig. S3). The starting material could be preliminarily indexed on the basis of an n = 2 term, with orthorhombic symmetry (space group *Cmc*21) (Ruiz-González *et al.*, 2015). As the oxygen content decreased, the corresponding patterns could be indexed again on the basis of an n = 2 term, suggesting a topotactic reduction process (Fig. S3). In spite of this similarity, some additional features, involving splitting and displacement of some reflections, were observed. Chemical homogeneity was checked by means of EDS and EPMA (Table S1). A nice fit with the nominal composition is obtained. This homogeneity was also confirmed by means of SAED which always displays the same characteristic patterns. The SAED study corresponding to the starting material $La_{0.5}Ca_{2.5}Mn_2O_7$ is in perfect agreement with XRD and ND studies since all patterns can be indexed on the basis of an n = 2 RP term (*Cmc*21) (Ruiz-González *et al.*, 2015). For the reduced samples, no changes are observed along $[0\bar{1}1]_o$ and $[010]_o$ (the subscript 'o' refers to the orthorhombic unit cell) zone axes, as observed in Figs. 1(*a*) and 1(*b*), respectively, corresponding to $La_{0.5}Ca_{2.5}Mn_2O_{6.5}$. Identical SAED patterns were obtained for the more reduced $La_{0.5}Ca_{2.5}Mn_2O_{6.25}$ sample (see Section S5 and Fig. S4).

As for the fully oxidized sample, no diffuse streaking was observed for any of the reduced samples, along the *a* axis, suggesting the absence of disordered intergrowths. This can be confirmed in the corresponding HRTEM image of $La_{0.5}Ca_{2.5}Mn_2O_{7-\delta}$, as depicted in Fig. 1(*c*), where periodicities of 0.39 × 1.93 nm, characteristic of the ordered intergrowth between one RS and two P layers, can be observed. In

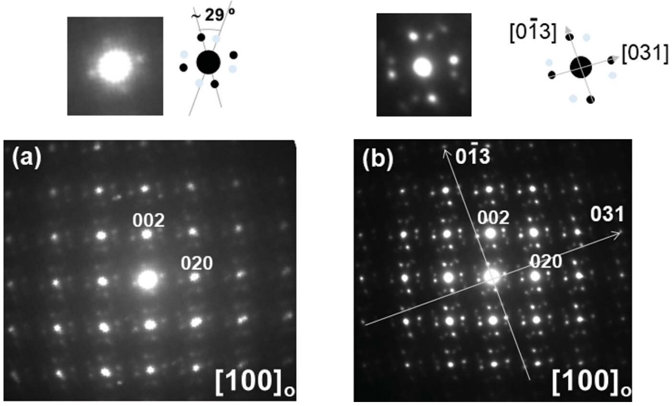

Figure 2
SAED pattern along [100], indexed according to the $Cmc2_1$ space group, characteristic of $La_{0.5}Ca_{2.5}Mn_2O_{6.5}$ (*a*) and $La_{0.5}Ca_{2.5}Mn_2O_{6.25}$ (*b*).

spite of this well ordered situation, additional reflections appear in the $[100]_o$ pattern [Figs. 2(*a*) and 2(*b*)]. In fact, eight diffuse reflections surround each basic spot as can be seen in the corresponding pattern of $La_{0.5}Ca_{2.5}Mn_2O_{6.5}$ [Fig. 1(*a*)]. They can be separated into two sets of reflections, along $[031]_o$ and equivalent directions, mutually rotated 29°, as more easily observed in the inset of Fig. 1(*a*), suggesting the presence of twinning. This fact, together with the diffuse nature of the reflections, could be related to the presence of small domains or nanoclusters of additional order in the material, indicating short-range ordering phenomena. For $La_{0.5}Ca_{2.5}Mn_2O_{6.25}$ [Fig. 2(*b*)], the situation is quite similar, but it should be emphasized that the additional reflections exhibit less diffuse character (see enhanced detail in the upper part of Fig. 2). In both cases, the periodicity in real space, corresponding to these reflections, is around 0.86 nm. Fig. 3(*a*) is a representative $La_{0.5}Ca_{2.5}Mn_2O_{6.25}$ HRTEM image along $[100]_o$. The corresponding fast Fourier transform (FFT) [Fig. 3(*b*)] is in agreement with the SAED patterns displayed in Fig. 2(*b*). The image shows the presence of three domains (A, B and C).

Domain A exhibits 0.27 × 0.27 nm periodicities characteristic of the $n = 2$ RP member, according to the corresponding FFT depicted in inset A. Domains B and C reflect the presence of identical superlattices, 0.86 × 0.86 nm, but mutually rotated 29°, as suggested by the SAED patterns [Figs. 2(*a*) and 2(*b*)] and confirmed in the corresponding FFTs (see corresponding B and C insets). These experimental results suggest that the appearance of the satellite reflections must be related to the accommodation of the oxygen vacancies on the basal plane since they become more evident as the oxygen content decreases, leading to a superstructure along $[031]_o$ and $[0\bar{1}3]_o$ and equivalent directions. This ideal new cell of dimensions 0.86 × 0.86 nm can be generated by eliminating the oxygen atoms along $[031]_o$ and $[0\bar{1}3]_o$, as schematically depicted in Fig. 3(*c*).

These sites involve removal of one equatorial oxygen atom from $[MnO_6]$ octahedra (marked in blue) along the drawn directions in the unit cell. It should be noticed that these positions belong to pure oxygen columns, *i.e.* they do not overlap with any cation of the structure along the [100] direction and can then be observed along this projection. Moreover, this modification would not have an influence on the *a* parameter. In this sense, the observed superlattice would be strictly related to the elimination of equatorial oxygen positions at the MnO layer. The order should be associated with a strong tendency for preferential elimination of the oxygen atoms from those sites marked in Fig. 3(*c*), providing additional spots in the SAED pattern (Fig. 2) and the superlattice detected in the HRTEM image (Fig. 3). This ideal model is the same as that described in the oxygen-deficient perovskite $CaMnO_{2.8}$ (Reller *et al.*, 1984) although the observed superlattice (Fig. 3) and the extra spots (Fig. 2) are comparatively much more diffuse due to the fact that there are two P layers alternating with one RS type. Nevertheless, since the oxygen content of the sample is lower (see Section S5.2 in the supporting information), additional oxygen atoms should be randomly removed from their sites. This disorder explains the diffuse character of the spots and periodicities in the SAED pattern and HRTEM image, respectively.

The appearance of similar satellite reflections has already been described in $La_{2-2x}Ca_{1+2x}Mn_2O_7$ ($0.6 < x < 0.8$). (Fawcett *et al.*, 2000; Bendersky *et al.*, 2004). However, their interpretation differs from ours, since those spots were assumed to be an incommensurate modulation probably related to either La–Ca cationic order or the Mn^{3+}–Mn^{4+} CO state, even when they appear on a sample exhibiting a slight oxygen deficiency (see Section S5.2 in the supporting information). On the other hand, the appearance of additional reflections in the MnO_2 layer accounting for a superstructure has also been reported in the reduced $n = 2$ RP $Sr_3Mn_2O_6$ compound (Gillie *et al.*, 2003), based on previous observations in the $n = 1$ related $Sr_2MnO_{3.5+\sigma}$ (Gillie *et al.*, 2002). Nevertheless, in this case they appear along $[010]_o$ and $[001]_o$ directions (according to our axes system) of the orthorhombic cell, instead of $[031]_o$ and $[0\bar{1}3]_o$ observed here, leading to a new cell of $2a_o(2)^{1/2} \times 2a_o(2)^{1/2}$ parameters on the basal MnO_2 plane. In this case, the

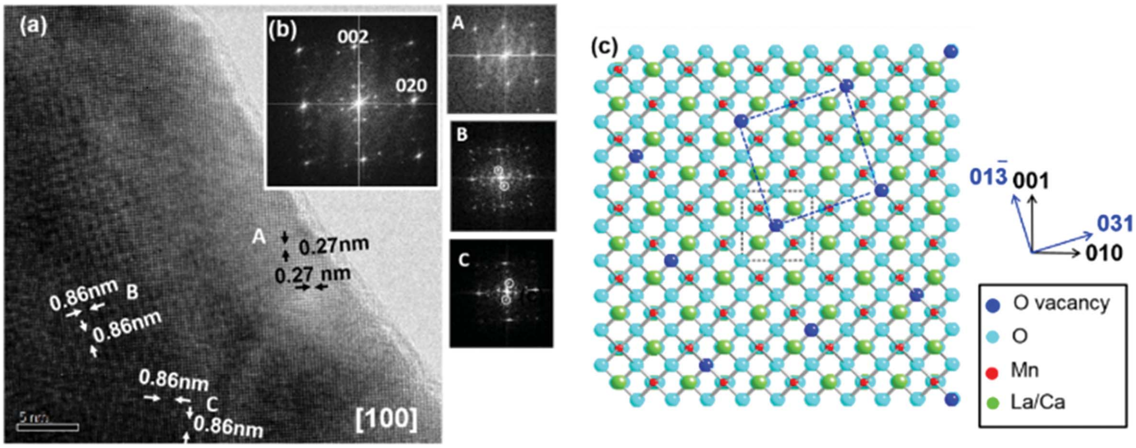

Figure 3

(*a*) HRTEM image corresponding to $La_{0.5}Ca_{2.5}Mn_2O_{6.25}$ along $[100]_o$ showing the presence of three domains marked as A, B and C (corresponding FFTs are displayed as insets). (*b*) FFT corresponding to the whole area. (*c*) Schematic atomic model, along $[100]_o$. A new hypothetical cell, as a consequence of the ordering of the O vacancies along $[031]_o$ and $[0\bar{1}3]_o$ perpendicular directions, is marked in navy blue.

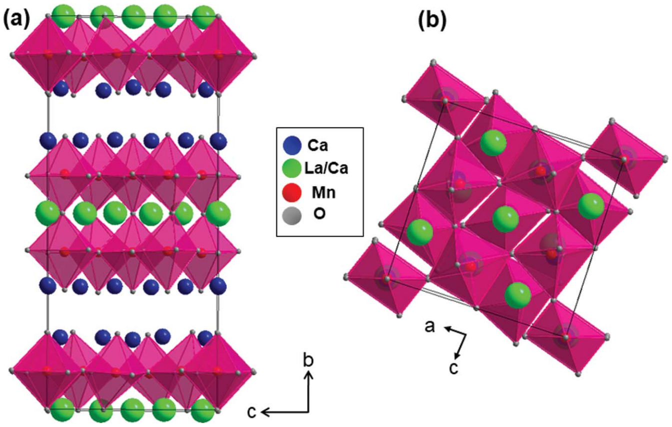

Figure 4
Structural model of $La_{0.5}Ca_{2.5}Mn_2O_{6.25}$ unit cell along (*a*) $[10\bar{1}]_m$ and (*b*) $[010]_m$.

superlattice was not detected by XRD but shown by SAED, as in our case, and, again, it was almost invisible to the eye in the HRTEM image. Starting from the new superstructure based on oxygen elimination along $[010]_o$ and $[001]_o$ directions, their ND analysis led to a non-fully ordered model.

According to this information and in order to complete the structural knowledge, we have performed an ND study on the basis of a new RP cell which includes the detected ordering along $[031]_o$ and $[0\bar{1}3]_o$ (see Section S6 and Fig. S5). In addition, La is always in 12 coordination in the P block while Ca occupies both the P and RS sites, according to the atomically resolved high-angle annular dark-field (HAADF) and electron energy-loss spectroscopy (EELS) mapping study (see Section S7 and Fig. S8). This has been done for $La_{0.5}Ca_{2.5}Mn_2O_{6.25}$ since satellite reflections appearing on the SAED pattern and the corresponding HRTEM image are sharper than in those corresponding to the more oxidized $La_{0.5}Ca_{2.5}Mn_2O_{6.5}$. The new parameters ($a_n$, b_n and c_n), in relation to the starting unit cell (a_o, b_o and c_o) (Ruiz-González *et al.*, 2015), are given by: $a_n = a_o = 1.99$ nm, $b_n = [(3/2b_o)^2 + (1/2c_o)^2]^{1/2} = 0.85$ nm and $c_n = [(1/2b_o)^2 + (3/2c_o)^2]^{1/2} = 0.85$ nm. In order to simplify the refinement, the less distorted $Sr_3Mn_2O_7$ unit cell (Gillie *et al.*, 2003) was used as the starting point (see Section S6). The starting model was built by expanding and transforming the structural base so as to fit the proposed cell from SAED data. The resulting unit cell was analysed with the aid of the *FINDSYM* program (Stokes & Hatch, 2005) to explore compatible symmetries, with the monoclinic $P2/m$ found to be the most plausible space group. It should be emphasized that the distortion angle is very small, 89.9°, just slightly different to the orthorhombic one (see Fig. S7). The resulting structural model was taken as the starting point for the Rietveld refinement carried out on powder ND data by means of the *Fullprof* program (Rodríguez-Carvajal, 1993). The resulting structure from Rietveld refinement of the ND data is depicted in Fig. 4 along a_m and b_m directions. Note that, according to Section S6 and Fig. S6, a new axes system is adopted. The octahedral distortion (see table of distances and bond angles in Section S6), even when already present in the starting material $La_{0.5}Ca_{2.5}Mn_2O_7$ (Ruiz-González *et al.*, 2015), is more noticeable here. This result is reasonable because, apart from the different occupation by La and Ca at the *A* site of the P blocks, which could be responsible for local differences in the octahedral tilt, the introduction of anionic vacancies gives rise to the reduction of the Mn oxidation state. Actually, for $La_{0.5}Ca_{2.5}Mn_2O_{6.25}$, the nominal Mn oxidation state is Mn^{3+} which exhibits strong Jahn–Teller character. For a better understanding, an additional representation of the unit cell indicating the different occupancy of each O has been included in Fig. S6.

These oxygen vacancies lead to the appearance of a very short-range ordered array, in the MnO_2 layers of the P block, of corner-connected Jahn–Teller distorted MnO_5 square-based pyramids. In fact, this situation could be related to the diffuse extra reflections in SAED patterns.

Finally, taking into account the resulting model for $La_{0.5}Ca_{2.5}Mn_2O_{6.25}$, we have performed image calculations (see Figs. S13 and S14) along different zone axes. For $La_{0.5}Ca_{2.5}Mn_2O_{6.5}$, an intermediate situation between $La_{0.5}Ca_{2.5}Mn_2O_7$ and $La_{0.5}Ca_{2.5}Mn_2O_{6.25}$ is expected according to the diffuse nature of the additional spots which suggests a more random distribution of the oxygen vacancies. This is also in agreement with XRD and ND data.

Annular bright-field (ABF) imaging in STEM (scanning transmission electron microscopy) is a robust method for observing light atoms like oxygen (see Section S7) (Findlay *et al.*, 2009, 2010). Furthermore, the potential of this

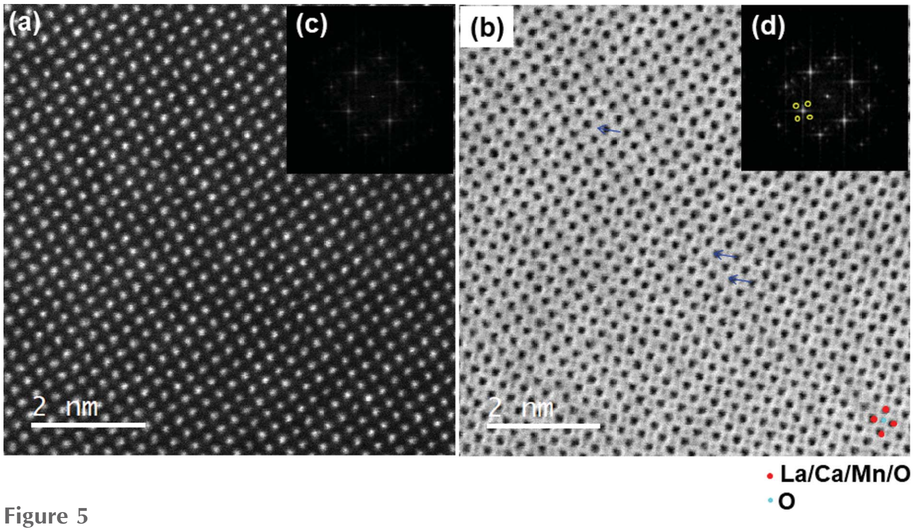

Figure 5
(*a*) HAADF image along $[100]_o$. (*b*) Corresponding ABF image. Atomic columns of overlapping La/Ca/Mn/O and pure O are represented in red and blue, respectively. Blue arrows indicate sites of a probably lower O occupancy or anionic vacancies. (*c*) FFT of the HAADF image and (*d*) FFT of the ABF image.

technique makes it possible to study defect structures related to oxygen vacancies (Hojo *et al.*, 2010; Kobayashi *et al.*, 2012; Lee, Oshima *et al.*, 2011). In our case, an ABF study has been performed along $[0\bar{1}1]_o$ and $[100]_o$. Along $[0\bar{1}1]_o$, ABF images do not evidence oxygen deficiency ordering (see Fig. S9) for $La_{0.5}Ca_{2.5}Mn_2O_{6.5}$ and $La_{0.5}Ca_{2.5}Mn_2O_{6.25}$. In the perpendicular direction, characteristic HAADF and ABF images, simultaneously acquired, are shown in Fig. 5. In the HAADF image [Fig. 5(*a*)], only the heaviest-atom columns are visible. Along this projection, no distinction between Mn and La/Ca is possible since they overlap. Nevertheless, in this projection, as already discussed, there are pure oxygen columns, but they are not visible in the HAADF condition. They become apparent on the ABF image [Fig. 5(*b*)]. In this image, both heavy (La, Ca and Mn) and light (O) atoms appear as darker spots on a brighter background. The cations appear as black and the O atoms, of smaller size, as grey (see the ball model at the bottom right-hand side). Even when the image does not reflect a long-range-ordered structure, based on the presence of a well defined ordered anionic vacancy pattern, the contrast of the O-atom columns changes and there are places where it almost disappears (marked by arrows), reasonably accounting for differences in the O occupation, in agreement with the ND refinement. Different intensities can be observed along line profiles of oxygen columns in Section S7 and Fig. S10. Finally, the FFTs of the HAADF [Fig. 5(*c*)] and ABF [Fig. 5(*d*)] show interesting differences. In the FFT corresponding to the HAADF, the reflections accounting for the superlattice do not appear clearly, as happens in $SrMnO_{2.6}$ (Kobayashi *et al.*, 2012), while they are present in the ABF. This situation can be better observed in the lower-resolution images depicted in Fig. S11.

The ensemble of these data supports a topotactic reduction of starting $La_{0.5}Ca_{2.5}Mn_2O_7$ through complex ordering of anionic vacancies in nanoclusters occurring in preferential oxygen sites in the $[MnO_2]$ plane along $[031]_o$ and $[0\bar{1}3]_o$. Apart from these structural features, a gradual decrease of the average Mn oxidation state in the three samples, with different oxygen content, has been followed using EELS (see Section S7). For $La_{0.5}Ca_{2.5}Mn_2O_7$ and $La_{0.5}Ca_{2.5}Mn_2O_{6.5}$, Mn^{4+} and Mn^{3+} coexist in different amounts according to the nominal composition, while in $La_{0.5}Ca_{2.5}Mn_2O_{6.25}$, only Mn^{3+} is present, as expected. Regarding the magnetic behaviour, the reduction process in $La_{0.5}Ca_{2.5}Mn_2O_{7-\delta}$ gives rise to the disappearance of the CO state at 283 K and also to a decrease in the ferromagnetic (FM) fluctuations at high temperature (Fig. 6). The introduction of anionic vacancies in $La_{0.5}Ca_{2.5}Mn_2O_7$ (Ruiz-González *et al.*, 2015) involves the reduction of Mn^{4+} and the transformation of octahedra into square pyramids, inducing the breaking of Mn^{4+}–Mn^{3+} FM interactions by the double exchange (DE) mechanism. Furthermore, since only Mn^{3+} is present in $La_{0.5}Ca_{2.5}Mn_2O_{6.25}$, DE interactions are not possible and, therefore, the superexchange ones lead to AFM behaviour. In the same way, the Curie–Weiss temperature decreases from $\theta \simeq -86$ K for $La_{0.5}Ca_{2.5}Mn_2O_7$ to $\theta \simeq -290$ K for both reduced samples. In the low-temperature region, an appreciable increase of the magnetization moment is observed [Figs. 6(*a*) and 6(*b*)]. This increase is in agreement with the higher ratio of Mn^{3+}, as the oxygen content is reduced. From these data, it can be concluded that, at low temperature, the AFM behaviour is reinforced [Fig. 6(*b*)]. The reduction process gives rise to the decrease in FM interactions reinforcing the AFM ones at low temperature (Fig. 6). Moreover, the spin-canting effect in the magnetic structure must be strengthened, as can be deduced from Fig. 6 where the ZFC (zero field cooling) and FC (field cooling) curves diverge at temperatures lower than 60 K. This effect is in agreement with the higher orthorhombic distortion of the structure as the anionic vacancies are introduced.

Electrical conductivity (σ) measurements have been performed using impedance spectroscopy in wide frequency and temperature ranges under an inert atmosphere to avoid sample oxidation. The conductivity values at room temperature for the pristine $La_{0.5}Ca_{2.5}Mn_2O_7$ sample and the reduced $La_{0.5}Ca_{2.5}Mn_2O_{6.5}$ and $La_{0.5}Ca_{2.5}Mn_2O_{6.25}$ oxides are 3×10^{-2}, 5×10^{-3} and 6×10^{-5} S cm^{-1}, respectively. The $La_{0.5}Ca_{2.5}Mn_2O_{7-\delta}$ oxygen-deficient phases display conductivity changes induced by the electron doping effect associated

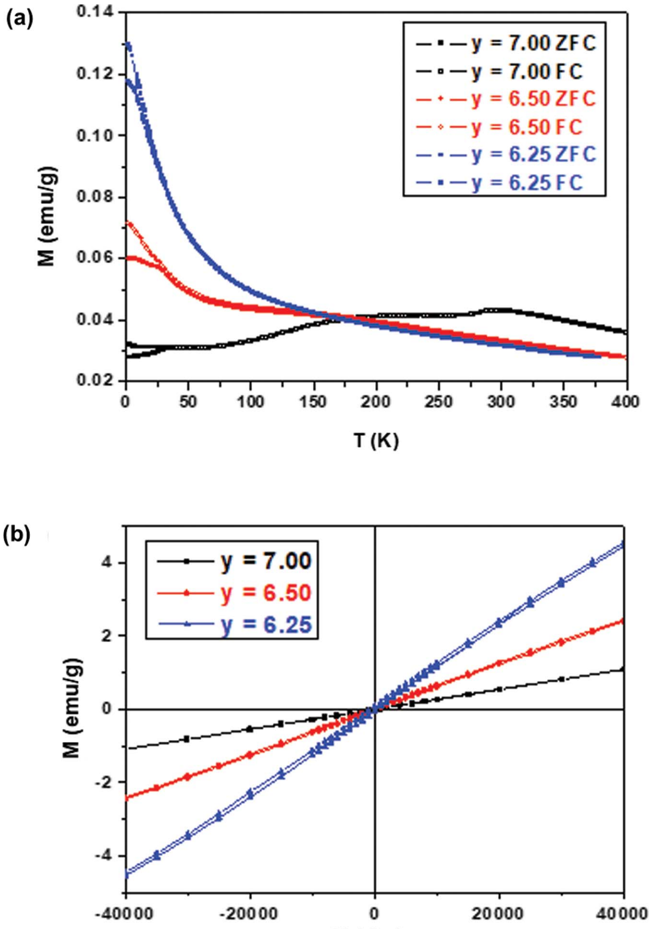

Figure 6

(*a*) Magnetization curves versus temperature for $La_{0.5}Ca_{2.5}Mn_2O_{6.5}$ and $La_{0.5}Ca_{2.5}Mn_2O_{6.25}$ in comparison with $La_{0.5}Ca_{2.5}Mn_2O_7$ starting material, under 1000 Oe applied field. (*b*) Magnetization curves versus the applied magnetic field at 5 K for $La_{0.5}Ca_{2.5}Mn_2O_{6.5}$ and $La_{0.5}Ca_{2.5}Mn_2O_{6.25}$ in comparison with $La_{0.5}Ca_{2.5}Mn_2O_7$ starting material.

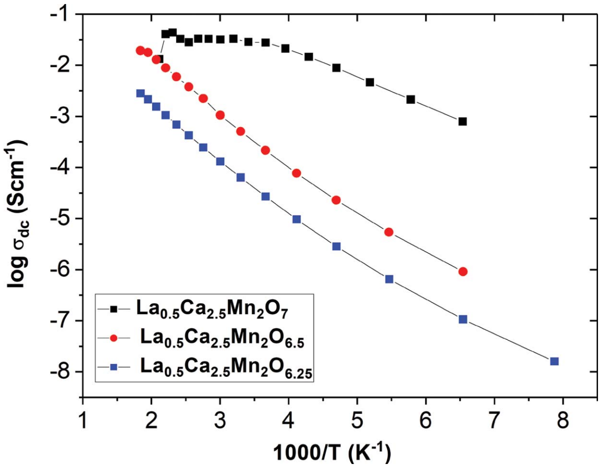

Figure 7
Representation of DC conductivity versus temperature for $La_{0.5}Ca_{0.5}Mn_2O_7$, $La_{0.5}Ca_{0.5}Mn_2O_{6.5}$ and $La_{0.5}Ca_{0.5}Mn_2O_{6.25}$.

with the oxygen vacancy nanoclusters created in the original [MnO_2] layer. The temperature-dependent DC conductivity obtained from the low-frequency admittance plateaus displays semiconductor behaviour (Fig. 7), similarly to that previously observed in the starting material $La_{0.5}Ca_{2.5}Mn_2O_7$ (Toyoda *et al.*, 2011). On the other hand, the activation energy (E_a) values for $La_{0.5}Ca_{2.5}Mn_2O_7$, $La_{0.5}Ca_{2.5}Mn_2O_{6.5}$ and $La_{0.5}Ca_{2.5}Mn_2O_{6.25}$ compounds are ~0, 0.18 and 0.22 eV, respectively. The small E_a observed for the pristine sample above room temperature is probably related to residual DE above the CO transition, which occurs close to room temperature in this compound. A decrease of the conductivity along with an increase of the activation energy is observed upon oxygen removal, suggesting a degree of hole carrier compensation resulting from the electron generation, although we cannot exclude the fact that reduced mobility results from the confinement of electronic carriers in the nanoclusters of oxygen-deficient MnO_x sheets. Notice that the fingerprint of the CO transition at high temperature is not observed in the oxygen-deficient samples, indicating that it is suppressed as a result of the decrease in Mn^{4+}. This would be consistent with the suppression of the FM fluctuations which are observed in the pristine sample above the CO transition but also disappear in the reduced samples. It is worth mentioning that, for $La_{0.5}Ca_{2.5}Mn_2O_{6.25}$, the E_a value is similar to the one observed for $LaMnO_3$, both exhibiting only Mn^{3+} (Nath *et al.*, 2013).

4. Conclusions

The ensemble of the above experimental results allows us to propose a topotactic reduction process, $La_{0.5}Ca_{2.5}Mn_2O_7 \rightarrow La_{0.5}Ca_{2.5}Mn_2O_{6.5} \rightarrow La_{0.5}Ca_{2.5}Mn_2O_{6.25}$, not studied in this system until now, in which the $n = 2$ RP basic skeleton is kept, while oxygen vacancies are preferably accommodated in small clusters or rotated domains on the basal plane along [031] and equivalent directions, instead of along [011] as shown in related $n = 2$ RP systems. Atomically resolved HAADF and EELS techniques show the short-range order–disorder phenomena of La and Ca cations for all oxygen stoichiometries, underlying the topotactic nature of the reduction process. The *A* site of RS layers is always occupied by Ca while La is always at the *A* site of the P blocks randomly alternating with additional Ca. The Mn oxidation state gradually decreases from Mn^{4+} and Mn^{3+}, in the starting sample, to Mn^{3+} in the more reduced one, resulting in $n = 2$ RP phases with a wider range of Mn oxidation states than in other related systems previously studied. The gradual decrease of the Mn oxidation state, accommodated by short-range ordering of anionic vacancies, reasonably explains the breaking of FM interactions reinforcing the AFM ones. The introduction of anionic vacancies results in hole compensation due to the decrease of Mn^{4+} which also gives rise to the suppression of the CO transition observed in the pristine sample at room temperature. Nevertheless, we should mention the slight increase of the E_a for $La_{0.5}Ca_{2.5}MnO_{6.25}$, which could be related to the effect of the oxygen vacancy nanoclusters. These new crystal-chemical and redox features of the $La_{0.5}Ca_{2.5}Mn_2O_{7-\delta}$ system reported here provide the basis for research into the functional properties of $n = 2$ RP manganites.

5. Related literature

Related literature cited in the supporting information: Bonnet *et al.* (1999), Cortés-Gil *et al.* (2016), Egerton (1993), González-Jiménez *et al.* (2014) and Suescun *et al.* (2007).

Acknowledgements

We are grateful to Dr E. Suard for assistance at ILL. We thank the National Center of Electron Microscopy (UCM) for facilities. Scientific discussions and support provided by Drs E. Okunishi and H. Sawada (JEOL Ltd Co.) are acknowledged.

Funding information

This work was supported by the Spanish Ministry of Innovation, Science and Technology and the Spanish Ministry of Economy and Competitiveness through Research Projects CSD2009-00013, TSI-020100-2011-280, MAT2011-23068, MAT2012-37109-C02-01 and MAT2014-52405-C02-01, and by the Madrid Regional Program through grant CAM S2013/MIT-2740.

References

Battle, P. D., Cox, D. E., Green, M. A., Millburn, J. E., Spring, L. E., Radaelli, P. G., Rosseinsky, M. J. & Vente, J. F. (1997). *Chem. Mater.* **9**, 1042–1049.

Battle, P. D., Green, M. A., Laskey, N. S., Millburn, J. E., Murphy, L., Rosseinsky, M. J., Sullivan, S. P. & Vente, J. F. (1997). *Chem. Mater.* **9**, 552–559.

Bendersky, L. A., Fawcett, I. D. & Greenblatt, M. (2004). *Chem. Mater.* **16**, 5304–5310.

Bonnet, N., Brun, N. & Colliex, C. (1999). *Ultramicroscopy*, **77**, 97–112.

Cortés-Gil, R., Ruiz-González, M. L., González-Merchante, D., Alonso, J. M., Hernando, A., Trasobares, S., Vallet-Regí, M., Rojo, J. M. & González-Calbet, J. M. (2016). *Nano Lett.* **16**, 760–765.

Dann, S. E. & Weller, M. T. (1995). *J. Solid State Chem.* **115**, 499–507.

Egerton, R. F. (1993). *Electron Energy-loss Spectroscopy in the Electron Microscope*. New York: Plenum.

El Shinawi, H., Bertha, A., Hadermann, J., Herranz, T., Santos, B., Marco, J. F., Berry, F. J. & Greaves, C. (2010). *J. Solid State Chem.* **183**, 1347–1353.

Fawcett, I. D., Kim, E., Greenblatt, M., Croft, M. & Bendersky, L. A. (2000). *Phys. Rev. B*, **62**, 6485–6495.

Findlay, S. D., Shibata, N., Sawada, H., Okunishi, E., Kondo, Y. & Ikuhara, Y. (2010). *Ultramicroscopy*, **110**, 903–923.

Findlay, S. D., Shibata, N., Sawada, H., Okunishi, E., Kondo, Y., Yamamoto, T. & Ikuhara, Y. (2009). *Appl. Phys. Lett.* **95**, 191913.

Gillie, L. J., Wright, A. J., Hadermann, J., Van Tendeloo, G. & Greaves, C. (2002). *J. Solid State Chem.* **167**, 145–151.

Gillie, L. J., Wright, A. J., Hadermann, J., Van Tendeloo, G. & Greaves, C. (2003). *J. Solid State Chem.* **175**, 188–196.

González-Jiménez, I. N., Torres-Pardo, A., Sánchez-Peláez, A. E., Gutiérrez, A., García-Hernández, M., González-Calbet, J. M., Parras, M. & Varela, A. (2014). *Chem. Mater.* **26**, 2256–2265.

Hayward, M. A. (2006). *Chem. Mater.* **18**, 321–327.

Hayward, M. A. (2014). *Semicond. Sci. Technol.* **29**, 064010.

Hojo, H., Mizoguchi, T., Ohta, H., Findlay, S. D., Shibata, N., Yamamoto, T. & Ikuhara, Y. (2010). *Nano Lett.* **10**, 4668–4672.

Jeyalakshmi, V., Mahalakshmy, R., Ramesh, K., Rao, P. V. C., Choudary, N. V., Sri Ganesh, G., Thirunavukkarasu, K., Krishnamurthy, K. R. & Viswanathan, B. (2015). *RSC Adv.* **5**, 5958–5966.

Kobayashi, S., Findlay, S., Shibata, N., Mizoguchi, T., Sato, Y., Okunishi, E., Ikuhara, Y. & Yamamoto, Y. (2012). *Appl. Phys. Lett.* **100**, 193112.

Lee, C. H., Orloff, N. D., Birol, T., Zhu, Y., Goian, V., Rocas, E., Haislmaier, R., Vlahos, E., Mundy, J. A., Kourkoutis, L. F., Nie, Y., Biegalski, M. D., Zhang, J., Bernhagen, M., Benedek, N. A., Kim, Y., Brock, J. D., Uecker, R. L., Xi, X. X., Gopalan, V., Nuzhnyy, D., Kamba, S., Muller, A., Takeuchi, I., Booth, J. C., Fennie, C. J. & Schlom, D. G. (2013). *Nature*, **502**, 532–536.

Lee, J., Kao, C. C., Nelson, C. S., Jang, H., Ko, K. T., Kim, S. B., Choi, Y. J., Cheong, S. W., Smadici, S., Abbamonte, P. & Park, J. H. (2011). *Phys. Rev. Lett.* **107**, 037206.

Lee, J. H., Luo, G., Tung, I. C., Chang, S. H., Luo, Z., Malshe, M., Gadre, M., Bhattacharya, A., Nakhmanson, S. M., Eastman, J. A., Hong, H., Jellinek, J., Morgan, D., Fong, D. D. & Freeland, J. W. (2014). *Nat. Mater.* **13**, 879–883.

Lee, S., Oshima, Y., Sawada, H., Hosokawa, F., Okunishi, E., Kaneyama, T., Kondo, Y., Niitaka, S., Takagi, H., Tanishiro, Y. L. & Takayanagi, K. (2011). *J. Appl. Phys.* **109**, 113530.

Ling, C. D., Millburn, J. E., Mitchell, J. F., Argyriou, D. N., Linton, J. & Bordallo, H. N. (2000). *Phys. Rev. B*, **62**, 15096–15111.

Lucas, S., Caignaert, V., Hervieu, M., Michel, C. & Raveau, B. (1992). *Eur. J. Solid State Inorg. Chem.* **29**, 399–409.

Massee, F., de Jong, S., Huang, Y., Siu, W. K., Santoso, I., Mans, A., Boothroyd, A. T., Prabhakaran, D., Follath, R., Varykhalov, A., Patthey, L., Shi, M., Goedkoop, J. B. & Golden, M. S. (2011). *Nat. Phys.* **7**, 978–982.

Millburn, J. E. & Mitchell, J. F. (2001). *Chem. Mater.* **13**, 1957–1966.

Mitchell, J. F., Millburn, J. E., Medarde, M., Short, S., Jorgensen, J. D. & Fernández-Díaz, M. T. (1998). *J. Solid State Chem.* **141**, 599–603.

Moritomo, Y., Asamitsu, A., Kuwahara, H. & Tokura, Y. (1996). *Nature*, **380**, 141–144.

Mulder, A. T., Benedek, N. A., Rondinelli, J. M. & Fennie, C. J. (2013). *Adv. Funct. Mater.* **23**, 4810–4820.

Nath, R., Raychaudhuri, A. K., Mukovskii, Y. M., Mondal, P., Bhattacharya, D. & Mandal, P. (2013). *J. Phys. Condens. Matter*, **25**, 155605.

Nguyen, N., Er-Rakho, L., Michel, C., Choisnet, J. & Raveau, B. (1980). *Mater. Res. Bull.* **15**, 891–897.

Poeppelmeier, K. R., Leonowicz, M. E. & Longo, J. M. (1982). *J. Solid State Chem.* **44**, 89–98.

Reller, A., Thomas, J. M., Jefferson, D. A. & Uppal, M. K. (1984). *Proc. R. Soc. London Ser. A*, **394**, 223–241.

Rijnders, G. (2014). *Nat. Mater.* **13**, 844–845.

Rodríguez-Carvajal, J. (1993). *Physica B*, **192**, 55–69.

Ruiz-González, L., González-Merchante, D., Cortés-Gil, R., Alonso, J. M., Martínez, J. L., Hernando, A. & González-Calbet, J. M. (2015). *Chem. Mater.* **27**, 1397–1404.

Stokes, H. T. & Hatch, D. M. (2005). *J. Appl. Cryst.* **38**, 237–238.

Suescun, L., Chmaissem, O., Mais, J., Dabrowski, B. & Jorgensen, J. D. (2007). *J. Solid State Chem.* **180**, 1698–1707.

Toyoda, T., Sasaki, N., Shimada, K., Okube, M. & Sasaki, S. (2011). *Jpn. J. Appl. Phys.* **50**, 041101.

Viciu, L., Zandbergen, H. W., Xu, Z., Huang, Q., Lee, M. & Cava, R. J. (2006). *J. Solid State Chem.* **179**, 500–511.

Yan, L., Niu, H., Bridges, C. A., Marshall, P. A., Hadermann, J., van Tendeloo, G., Chalker, P. R. & Rosseinsky, M. J. (2007). *Angew. Chem. Int. Ed.* **46**, 4539–4542.

Zurita-Blasco, M. D., Attidekou, P. S. & Wright, A. J. (2007). *J. Mater. Chem.* **17**, 923–930.